Plasmons in isolated single-walled carbon nanotubes

Plasmons in isolated single-walled carbon nanotubes

Ricardo Perez and William Que

Department of Physics, Ryerson University, 350 Victoria Street, Toronto, ON, M5B 2K3, Canada

E-mail: rtperez@scs.ryerson.ca

Abstract
The collective excitation modes of individual single-walled carbon nanotubes are studied theoretically in the nearest-neighbour tight-binding approximation. Umklapp terms are taken into account and local-field effects are studied. Plasmon mode dispersion relations for carbon nanotubes with radius $R \sim 7$ Å are obtained. We report a strong dependence of the plasmon dispersion on the chirality of the carbon nanotubes. In particular, armchair and zigzag tubes have dispersive plasmons, but some of the chiral tubes have essentially dispersionless plasmons. Our results offer an alternative explanation to the origin of the experimentally observed low-energy dispersionless modes found in momentum-dependent EELS experiments. Important differences between a tight-binding model and free electron gas model are discussed and it is shown that some important qualitative features cannot be captured by a free electron gas model. An acoustic plasmon mode is found in all metallic carbon nanotubes, giving support to the experimental findings in Raman scattering.

(Some figures in this article are in colour only in the electronic version)

1. Introduction

For over a decade, since the pioneering article by Iijima [1], carbon nanotubes have been at the centre of attention of the scientific community due to their rich electronic and optical properties and to their potential applications. Intensive research efforts have allowed us to have a good understanding of some of the basic properties of carbon nanotubes [2, 3]. The electronic single-particle band structures are well described by the tight-binding model. Collective vibrational modes have been studied extensively by Raman scattering and the different modes and their line shapes have been identified and well explained. In contrast, our present understanding of collective electronic excitation modes or plasmons in carbon nanotubes is still very limited.

The majority of experimental investigations of plasmons in carbon nanotubes are electron energy loss spectroscopy (EELS) studies [4–15]. EELS experiments have been carried out in samples of multi-wall nanotubes (MWNTs), single-wall nanotubes (SWNTs) and their bundles.

Reed and Sarikaya [10] offered a detailed analysis of the obtained experimental outcomes, pointing out that some of the results and interpretations have been contradictory.

Raman scattering experiments studying phonons in carbon nanotubes have also provided insights on plasmons indirectly [16, 17]. In addition, reflectivity measurements by Bommeli *et al* [18] have suggested a plasmon energy of 0.14 eV.

A large number of theoretical investigations of plasmons in carbon nanotubes are based on free electron gas models, by considering an electron gas confined to a cylindrical wall of either zero thickness or nonzero thickness [19–30]. MWNTs were modelled by several authors [19, 21, 22] as coaxial tubules of zero wall thickness. Jiang [24] used a two-fluid hydrodynamic description to model both π and σ electrons. Vasvari [25], and Taverna *et al* [29] considered cylindrical walls of finite thickness. Que [30] studied nanotube bundles whose cross section is a periodic 2D lattice.

Although the electron gas model is a good starting point for studying the qualitative features of plasmons in carbon nanotubes, its usefulness is limited. It is well known that the chirality of carbon nanotubes plays an important role in the electronic properties, and the band structures are dependent on the chiral vector, leading to metallic or semiconducting tubes. The plasmon excitations are expected to be dependent on the band structure. For example, one can expect to find acoustic plasmons in metallic nanotubes, but only optical plasmons can exist in semiconducting nanotubes. The electron gas model ignores such important fine details, and therefore, for quantitative detailed comparison with experiments, it is desirable to use better models that take into account the band structure of carbon nanotubes properly. Another drawback of the electron gas model is that it cannot assess the local-field effects [31, 32] associated with the periodic lattice structure.

Since the tight-binding model describes most of the carbon nanotube band structures very well, it is an excellent model beyond the electron gas description. So far, only Lin and co-workers [33–36] have used the tight-binding model for π electrons to obtain the loss functions for multi-wall carbon nanotubes, individual SWNTs and their bundles and graphite layers. Local-field effects were not included or assessed.

Very recently Marinopoulos *et al* [37, 38] performed *ab initio* density functional theory calculations of the optical and EELS spectra for single-walled carbon nanotube bundles of very small radius. Local-field effects were considered. They found that at the random phase approximation (RPA) level very good absorption spectra were obtained, suggesting that exchange–correlation effects are damped. The authors did not present any plasmon dispersion curves.

Inspired by the experimental possibilities to probe individual carbon nanotubes [10, 13, 14, 17, 39, 40], we present in this paper a detailed theoretical study of plasmons in individual SWNTs; the paper is intended to give all the details behind our previously obtained results [41]. We believe that studying individual carbon nanotubes is key to understand their electronic excitations, because experiments on bulk samples or bundles measure an average signal from many tubes of different chiralities and diameters, therefore many of the fine details are smeared out. There is already experimental evidence that the excitation energies in a bundle are different from those in a single tube, and different single tubes show individuality [10]. Our approach is similar to that used by Lin *et al*, using a tight-binding model for π electrons and the random phase approximation (RPA) to calculate the dielectric matrix; however, unlike Lin *et al*, we include the Umklapp terms in order to assess local-field effects [31, 32]. The same theoretical framework has been applied successfully to many systems including quantum wires [42]. We find that when all the Umklapp terms are dropped we obtain the same result as in the later papers of Lin *et al* [34, 35], hence confirming their results. We perform a detailed analysis of our results, and some of our findings have never appeared in the literature before. In

particular, we find that the plasmon dispersions can depend strongly on the chirality of carbon nanotubes. For nanotubes of similar radius, the armchair tubes and zigzag tubes both have significantly dispersive plasmons, but chiral (n, m) tubes whose greatest common denominator $\gcd(2n + m, 2m + n)$ is equal to unity have practically dispersionless plasmons. This and other predictions should fuel experimental efforts in our quest for the understanding of collective electronic excitations in carbon nanotubes.

The derivation of the dielectric matrix is sketched in section 2. Section 3 is devoted to introducing the tight-binding wavefunction relevant to the single-particle electronic states in the π and π^* bands. The obtained results are discussed in section 4 and conclusions are presented at the end. Three appendices are included, giving all the details of our calculations.

2. Dielectric matrix in SWNT

Consider an isolated SWNT of radius R and length ℓ. Assume a coordinate system with the z-axis being the nanotube's axis. The starting point for our derivation is the Poisson's equation for the induced potential $V_{in}(\vec{r})$ created by the induced electron density $n_{in}(\vec{r})$ due to the response of the system to the influence of an external potential.

The single-wall nanotube is a quasi-one-dimensional periodic system with a cylindrical symmetry and the electronic states are supposed to be confined in a small region near to its surface, then it is natural to consider that the system electronic excitations carry a well defined linear momentum q along the nanotube axis, and angular momentum L around it. Performing a Fourier transform along the nanotube axis and in the angular variable around it we obtain

$$V_{in}(\rho, L, q) = \frac{4e^2}{\ell \epsilon_0} \sum_{a,a'} \sum_{q',L'} \langle a | V(\rho', L', q') e^{-i(q'z'+L'\phi')} | a' \rangle$$
$$\times \langle a' | F(\rho', \rho, q, L) e^{i(|q|z'+L\phi')} | a \rangle \frac{f_0(E_{a'}) - f_0(E_a)}{E_{a'} - E_a + \omega}, \tag{1}$$

where $F(\rho', \rho, q, L) = I_L(|q|\rho_<)K_L(|q|\rho_>)$ and a, a' label the electron states described by the wavefunctions $\psi_a(\vec{r})$, $\psi_{a'}(\vec{r})$ with energies E_a, $E_{a'}$. The induced electron density is given within the self-consistent field approximation [43, 31, 32], and the appropriate expansion of the Coulomb potential in cylindrical coordinates as given in appendix A was used.

The induced potential in the surface of the nanotube can be fairly approximated by

$$V_{in}(R, L, q) = \frac{4}{\ell} V_R(q, L) \sum_{a,a'} \sum_{q',L'} V(R, L', q') \langle a | e^{-i(q'z'+L'\phi')} | a' \rangle$$
$$\times \langle a' | e^{i(|q|z'+L\phi')} | a \rangle \frac{f_0(E_{a'}) - f_0(E_a)}{E_{a'} - E_a + \omega}, \tag{2}$$

where the localized nature of the electronic states has been used and $V_R(q, L) = \frac{e^2}{\epsilon_0} F(R, R, q, L)$.

Introducing the response function

$$K(q, L; q', L'; \omega) = \frac{4}{\ell} \sum_{a,a'} \langle a | e^{-i(q'z'+L'\phi')} | a' \rangle \langle a' | e^{i(|q|z'+L\phi')} | a \rangle \frac{f_0(E_{a'}) - f_0(E_a)}{E_{a'} - E_a + \omega}, \tag{3}$$

then the dielectric matrix on the surface of the nanotube is given by the expression

$$\epsilon^R(q, L; q', L'; \omega) = \delta_{q,L;q',L'} - V_R(q, L) K(q, L; q', L'; \omega). \tag{4}$$

3. Single-particle electron states in an SWNT

The derivation in the previous section is the most general one. In this section we describe the model we will use for the single-particle electronic states associated with the π bands of an SWNT and apply it to obtain the corresponding expressions for the dielectric matrix and the macroscopic dielectric function.

As is well known, a single-wall carbon nanotube can be described using the so-called *zone folding method* as a graphene sheet rolled into a cylindrical shape. Let $\vec{C}_h = n\vec{a}_1 + m\vec{a}_2$ be the chiral vector, where n, m are integers and $\vec{a}_1, \vec{a}_2$ are the graphene lattice vectors. Let $\vec{T} = t_1\vec{a}_1 + t_2\vec{a}_2$ be the lattice vector of the 1D nanotube unit cell, where $t_1 = (2m + n)/d_R$, $t_2 = -(2n + m)/d_R$, and d_R is the greatest common divisor $d_R = \gcd(2n + m, 2m + n)$ [3]. Now, consider a strip along the $\vec{T}$ direction of length $\ell = N|\vec{T}|$ and width $w = |\vec{C}_h| = 2\pi R$. The strip can be described as a 1D Bravais lattice along the $\vec{T}$ direction with lattice period equal to $T = |\vec{T}|$ and unit cell determined by the vectors $\vec{C}_h$ and $\vec{T}$. Note that if the strip is repeated periodically with the period given by the $\vec{C}_h$ vector, we reconstruct the graphene plane. The positions of the carbon atoms in the unit cell are given by the vector $\vec{\tau}_\gamma = (\gamma - 1)\vec{R} - r_\gamma\vec{T}$, where the symmetry vector $\vec{R}$ is defined by the relation $\vec{R} = p_1\vec{a}_1 + p_2\vec{a}_2$, p_1, p_2 are the smallest integers that are solutions of the equation $t_1 p_2 - t_2 p_1 = 1$ with $\gcd(p_1, p_2) = 1$ and r_γ is an integer number which makes the necessary translations to restore the vectors $\vec{\tau}_\gamma$ inside the nanotube's unit cell [3]. The number of graphene unit cells within the strip unit cell is $N_0 = 2(m^2 + n^2 + nm)/d_R$ [3]. A useful property of the symmetry vector $\vec{R}$ is $N_0\vec{R} = \vec{C}_h + M\vec{T}$, where $M = mp_1 - np_2$. The strip reciprocal lattice vectors $\vec{K}_1, \vec{K}_2$ can be obtained from $\vec{C}_h$ and $\vec{T}$ in the usual way, with $\vec{K}_2$ parallel to the tube axis.

We use a nearest-neighbour tight-binding approximation to describe the single-particle electronic states of the system. The electron's wavefunctions are given by the expression

$$\psi_a(\vec{r}) = \psi_{\vec{k}}^h(\vec{r}) = \frac{1}{\sqrt{2}}[\Phi_{\vec{k}}^A(\vec{r}) + \lambda_{\vec{k}}^h \Phi_{\vec{k}}^B(\vec{r})], \tag{5}$$

where $\Phi_{\vec{k}}^{A,B}(\vec{r})$ are the tight-binding wavefunctions corresponding to atoms A and B in the graphene layer unit cell; their expression is

$$\Phi_{\vec{k}}^\alpha(\vec{r}) = \frac{1}{\sqrt{NN'}} \sum_{\beta=1}^{N} \sum_{\beta'=1}^{N'} e^{i\vec{k}\cdot(\vec{R}_\beta^\alpha + \vec{S}_{\beta'})} \frac{1}{\sqrt{N_0}} \sum_{\gamma=1}^{N_0} e^{i\vec{k}\cdot\vec{\tau}_\gamma} \phi_{2p_z}(\vec{r} - \vec{R}_\beta^\alpha - \vec{S}_{\beta'} - \vec{\tau}_\gamma), \tag{6}$$

where $\vec{R}_\beta^\alpha = (\beta - 1)\vec{T} + \delta_{\alpha,B}\vec{\ell}_{AB}$ and $\vec{S}_{\beta'} = (\beta' - 1)\vec{C}_h$, the functions $\phi_{2p_z}(\vec{r})$ are the $2p_z$ atomic orbitals of the π electrons in the carbon atoms and the $\vec{\ell}_{AB}$ vector gives the shifting from the lattice of A-type carbon atoms to the lattice of B-type atoms.

The Schrödinger equation is solved using the Slater–Koster [44] procedure and we obtain the eigenvalues

$$E_a = E_{\vec{k}}^h = (-1)^h \gamma_0 |f(\vec{k})|, \tag{7}$$

with the coefficients $\lambda_{\vec{k}}^h$ given by

$$\lambda_{\vec{k}}^h = (-1)^{h+1} \frac{f^*(\vec{k})}{|f(\vec{k})|} \tag{8}$$

and the function $f(\vec{k})$ comes from the structure of the underlying graphene lattice and is given by

$$f(\vec{k}) = e^{i\vec{k}\cdot(\frac{1}{3}\vec{a}_1 - \frac{2}{3}\vec{a}_2)} + e^{i\vec{k}\cdot(\frac{1}{3}\vec{a}_1 + \frac{1}{3}\vec{a}_2)} + e^{i\vec{k}\cdot(-\frac{2}{3}\vec{a}_1 + \frac{1}{3}\vec{a}_2)}. \tag{9}$$

In the previous expressions, $h = 0$ for electrons in the π band and $h = 1$ for electrons in the π^* band; the overlap integral is taken as $\gamma_0 = -3.03$ eV [45]. As a consequence of applying periodic boundary conditions in the direction of the chiral vector, the wavevectors $\vec{k}$ have the following form:

$$\vec{k} = \mu \vec{K}_1 + k \frac{\vec{K}_2}{|\vec{K}_2|} = \left(\frac{\mu}{R}, k \right), \tag{10}$$

where μ is an integer number from $\mu = 0$ to $N_0 - 1$, k belongs to the first Brillouin zone (1BZ) given by the interval $[-\pi/T, \pi/T]$ and the sum over β' can be eliminated from (6).

The edge of the 1BZ π/T for all nanotubes is equal to $\sqrt{3}d_R/6R$. Note that carbon nanotubes with approximately the same radius R but different chiralities have different Brillouin zone sizes; in particular, all armchair carbon nanotubes have $\pi/T = \pi/a$, with a being the lattice constant of the graphene sheet, and all zigzag carbon nanotubes have $\pi/T = \pi/(\sqrt{3}a)$. Taking $a = 2.49$ Å, we have $\pi/T = 1.26$ Å^{-1} for armchair nanotubes, and $\pi/T = 0.73$ Å^{-1} for zigzag nanotubes. Chiral nanotubes have $\pi/T = \pi d_R/(a\sqrt{3}(m^2 + n^2 + mn)) = 0.727 \gcd(2m + n, 2n + m)/\sqrt{m^2 + n^2 + mn}$ Å^{-1}. For those chiral tubes with $d_R = 1$, the Brillouin zone can be extremely small. As we will see later, this fact has important consequences for the dispersions of plasmon modes.

In the previous section it was shown how the dielectric matrix on the surface of the nanotube depends on the transfer momenta along the axis of the nanotube (q, q') and on the transfer angular momenta around it (L, L'). Using these magnitudes, and assuming that the geometry of the SWNT is locally flat, we can define a transfer momentum $\vec{q}$ on the graphene strip as

$$\vec{q} = L\vec{K}_1 + q \frac{\vec{K}_2}{|\vec{K}_2|} = \left(\frac{L}{R}, q \right), \tag{11}$$

and an analogous definition for $\vec{q}'$. The periodic nature of the nanotube allows us to consider any transfer momentum $\vec{q}$ as $\vec{q} = \vec{q}_0 + \vec{G}$, where $\vec{q}_0 = (\frac{L}{R}, q_0)$ with q_0 a wavevector in the 1BZ of the nanotube and $\vec{G} = g\vec{K}_2$ (g integer) is a vector in its reciprocal lattice. According to Bloch's theorem, the single-particle electronic states in a solid can be written in the form $\psi_{\nu \vec{k}}(\vec{r}) = \frac{1}{\sqrt{\Omega}} e^{i\vec{k}\cdot\vec{r}} u_{\nu \vec{k}}(\vec{r})$, where ν stands for all the quantum numbers other than $\vec{k}$ labelling the single-particle electronic states in the system, and Ω is the volume of the system. Using the property that the functions $u_{\nu \vec{k}}$ oscillate very rapidly within the unit cell, it is easy to show that

$$\langle \nu' \vec{k}' | e^{i\vec{q}\cdot\vec{r}} | \nu \vec{k} \rangle = \delta_{\vec{k}', \vec{k}+\vec{q}_0} \langle \nu' \vec{k} + \vec{q}_0 | e^{i(\vec{q}_0 + \vec{G})\cdot\vec{r}} | \nu \vec{k} \rangle.$$

Using the single-particle electronic states in the nanotube, described by the wavefunctions $\psi_{\vec{k}}^h(\vec{r})$, and with the help of the expressions above, we are able to compute the matrix element between the tight-binding functions of our model entering the definition of the response function K. The details are given in appendix B and the results are

$$\langle h' \vec{k}' | e^{i\vec{q}\cdot\vec{r}} | h\vec{k} \rangle = \delta_{\vec{k}', \vec{k}+\vec{q}_0} \delta_{gM, uN_0} \frac{1}{2} \left(1 + e^{i\vec{G}\cdot\vec{\ell}_{AB}} \lambda_{\vec{k}+\vec{q}_0}^{h'*} \lambda_{\vec{k}}^h \right) A(\vec{q}_0 + \vec{G}),$$

where the function $A(\vec{q})$ is given in appendix C. The response function is expressed as

$$K(q, L; q', L'; \omega) = \delta_{q_0, q_0'} \delta_{L, L'} \chi_{g, g'}(q_0, L, \omega)$$

where

$$\chi_{g, g'}(q_0, L, \omega) = \delta_{gM, uN_0} \delta_{g'M, u'N_0} A(\vec{q}_0 + g\vec{K}_2) A^*(\vec{q}_0 + g'\vec{K}_2) \Pi_{\vec{G}, \vec{G}'}(q_0, L, \omega), \tag{12}$$

and

$$\Pi_{\vec{G},\vec{G}'}(q_0, L, \omega) = \frac{1}{\ell} \sum_{h,h'} \sum_{\vec{k}} \frac{f_0(E^{h'}_{\vec{k}+\vec{q}_0}) - f_0(E^{h}_{\vec{k}})}{E^{h'}_{\vec{k}+\vec{q}_0} - E^{h}_{\vec{k}} + \omega} \left(1 + e^{i\vec{G}\cdot\vec{\ell}_{AB}} \lambda^{h'*}_{\vec{k}+\vec{q}_0} \lambda^{h}_{\vec{k}}\right)$$
$$\times \left(1 + e^{-i\vec{G}'\cdot\vec{\ell}_{AB}} \lambda^{h'}_{\vec{k}+\vec{q}_0} \lambda^{h*}_{\vec{k}}\right). \tag{13}$$

The expression of the response function leads us to a dielectric matrix which depends on a well defined transfer momentum q_0 and the angular momentum L

$$\epsilon_{g,g'}(q_0, L, \omega) = \delta_{g,g'} - V_R(q_0 + g|\vec{K}_2|, L)\chi_{g,g'}(q_0, L, \omega), \tag{14}$$

and the macroscopic longitudinal dielectric function is obtained from it by means of the relation [31, 32]

$$\epsilon(q_0 + g|\vec{K}_2|, L, \omega) = \frac{1}{\left[\epsilon^{-1}(q_0, L, \omega)\right]_{g,g}}. \tag{15}$$

4. Results and discussion

The momentum-dependent EELS experiment carried out on bundles of SWNTs measures the loss function defined as the imaginary part of the inverse of the macroscopic dielectric function [7, 8, 11, 15, 12]. In the case of isolated nanotubes the experimental difficulties in achieving the resolution in momentum are enormous, thus available EELS spectra in this case have been measured using spatial resolution instead [13, 14, 29]. Macroscopic theoretical simulations, based on hydrodynamic and continuum dielectric models, for interpreting the results of this type of experiments have been presented and tested against the experimental results. In the case of momentum-dependent EELS, Marianopoulos *et al* [37, 38] argued that the spectrum of the nearly isolated nanotube case can be obtained from the bundle case in the limit of large lattice constant in the plane perpendicular to the nanotube axis and $q \to 0$. Lin *et al* have used the loss function obtained from the macroscopic dielectric function to study collective electronic excitations in isolated SWNTs and their bundles [33–36]. A closer study of this loss function will show up new aspects of the physics of the collective excitations in carbon nanotubes. Before proceeding to its calculation we note that if we do not take into account the Umklapp terms ($g, g' \neq 0$) then the expression given in (15), for the macroscopic dielectric function, exactly reproduces the result of Lin *et al* [34] for isolated SWNTs where no local-field effects were considered.

To analyse the local-field effects (LFEs) it is necessary to consider the Umklapp terms in the dielectric matrix, which, in principle, is of infinite dimension. The LFEs are determined by the nondiagonal elements in the dielectric matrix; all these elements contain the factor $A(\vec{q}_0 + g\vec{K}_2)A^*(\vec{q}_0 + g'\vec{K}_2)$, which has a finite value at $(g, g') = (0, 0)$ and goes to zero very rapidly as a function of g and g', as shown in figure 1, where it is plotted for the (10, 10) armchair nanotube with angular momentum $L = 0$ and transfer momentum along the nanotube axis $q_0 = 0.02$ Å^{-1}. There are no significant variations in this result for different values of L and q_0 as long as the radius of the considered nanotube is similar to the (10, 10)'s.

We have performed calculations using matrices with different dimensions to evaluate the effect of the nondiagonal elements of the dielectric matrix. Our results show that the effects of the local fields on the calculated loss functions are negligible at least for nanotubes with large radii ($R \sim 7$ Å), for which the *zone folding method* and the tight-binding model are good approximations. This supports the previous result of Benedict *et al* [46] that the component $\alpha_{0_{zz}}$ of the static polarizability is not affected by the effects of the local fields. They obtained
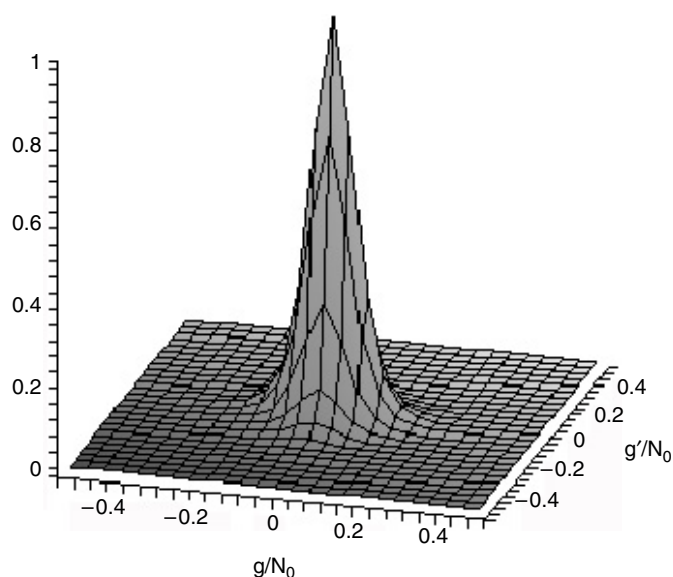
Figure 1. Factor $A(\vec{q}_0 + g\vec{K}_2)A^*(\vec{q}_0 + g'\vec{K}_2)$ as a function of scaled g and g' for the (10, 10) tube with angular momentum $L = 0$ and $q_0 = 0.02$ Å^{-1}.

their result using a classical approach in the long-wavelength limit ($q \rightarrow 0$). Our result can be seen as a generalization of their result to any value of the transfer momentum. Recent calculations [37, 38, 47] for the absorption spectra using different techniques (time-dependent density functional theory and Green's function approach) also support our findings in the long-wavelength regime.

Only for nanotubes with small values of n and m, like the (3, 3), (5, 0) and (4, 2) cases, do the off-diagonal terms of the dielectric matrix give a sizeable contribution, suggesting there could be non-negligible local-field effects; however, such tubes have a small radius ($R \sim 2$ Å) and the tight-binding model itself breaks down for these cases [2]. Marinopoulos *et al* [37, 38], have studied the local-field effects in the optical absorption spectra and EELS of bundles of these nanotubes, and they found that the significance of local-field effects depends on the direction of electric field polarization or momentum loss. When that direction is parallel (perpendicular) to the tube axis, the local-field effects are negligible (important).

In our calculation we took into account only the single-particle states for the π-electrons. The calculations were done for a variety of nanotubes including metallic and semiconducting tubes with similar radii $R \sim 7$ Å. Figure 2 shows the results for a typical loss function calculation for nanotubes (10, 10), (13, 7), (16, 3), (17, 0) and (18, 0) with radius R equal to 6.88, 6.98, 7.02, 6.75 and 7.14 Å; transfer momentum $q_0 = 0.04$ Å^{-1} and angular momenta $L = 0, 1, 2, 3$. The broadening used in these calculations was $\Gamma = 0.2$ eV, which is the value used in all our calculations from now on unless otherwise stated. Common features are that, for $L = 0$, there is a well defined peak at low energy with appreciable amplitude, which is identified as an acoustic plasmon mode for metallic nanotubes (see discussion below) and, for higher angular momentum, the first peak in the spectra is shifted to higher energies. For example, there is no distinguishable peak below 2 eV for excitations with angular momentum greater than two. This means that any collective mode with high angular momentum will be interpreted as an optical plasmon. The peaks with larger amplitude are shifted to energies in
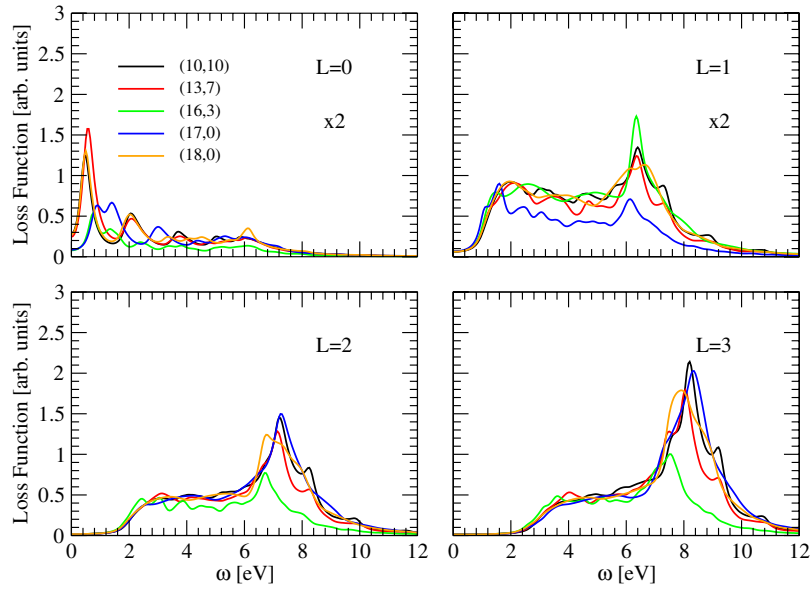
Figure 2. Loss function $\mathrm{Im}(-1/\epsilon(q_0, L, \omega))$ computed for $q_0 = 0.04$ Å^{-1} and different angular momenta for tubes with different chiralities but similar radius, about 7 Å.

the range 6–10 eV. The calculations were done for excitation energy up to 20 eV and we found that the spectra are featureless for ω larger than 12 eV for any transfer momentum in the 1BZ.

The fact that the loss functions are featureless above 12 eV is at first puzzling, but a detailed analysis of the expression for $\Pi_{\vec{G}, \vec{G}'}(q_0, L, \omega)$, given in (13), permits us to understand the numerical results. Figure 3 shows the band structure of the (10, 10) carbon nanotube. The Fermi level is at 0 eV. The subbands are pairwise mirror images of each other with respect to the Fermi level, with the outermost pair of subbands corresponding to quantum number $\mu = 0$, the innermost pair corresponding to quantum number $\mu = 10$, and other pairs in sequential order. An excitation from the lowest occupied subband to the highest empty subband could have an energy of about 18 eV. The corresponding allowed intersubband excitation would have at least this much energy, plus a depolarization shift. If we consider the energetics alone, we expect the loss functions to have features around such energies, but surprisingly the numerical results do not show such features. To understand this result we will consider the $\vec{G} = \vec{G}' = 0$ element; we note that in equation (13) there is not only the usual energy factor, but also an amplitude factor $|1 + \lambda_{\vec{k}+\vec{q_0}}^{h'*} \lambda_{\vec{k}}^{h}|^2$. For $\mu = 0$, we can show analytically that this amplitude factor is exactly equal to zero (because $f(\vec{k})$ is real in this case and $\lambda_{\vec{k}}^{h} = \pm 1$). The presence of the amplitude factor eliminates the contribution of the $\mu = 0$ subbands, and makes the contributions from other small μ subbands negligibly small, making the loss function featureless above 12 eV.

In figure 4 we show the different behaviours of the loss function of tubes with different chiralities as we vary the magnitude of the transfer momentum along the tube. The two upper panels in figure 4 show the loss functions for the metallic armchair (10, 10) tube with angular momenta $L = 0, 1$. For $L = 0$, at $q_0 = 0.02$ Å^{-1} there is a sharp peak at an energy below 1 eV; for higher values of q_0 the major peaks are shifted to excitation energies in the range 4–8 eV and the amplitude of the loss function clearly decreases as the transfer momentum goes to the edge of the Brillouin zone ($q_0 = 1.26$ Å^{-1}), this trend on the energy of the collective excitation
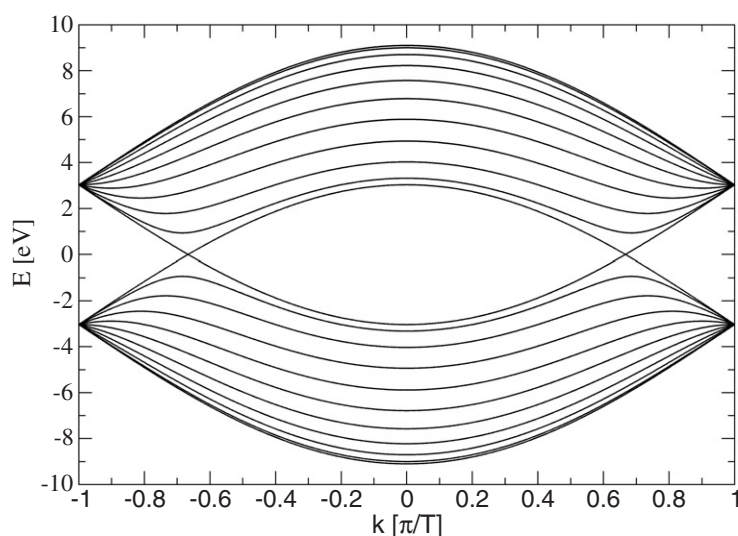
Figure 3. Band structure of the armchair (10, 10) carbon nanotube within the tight-binding model. Subbands above and below the Fermi level $E_F = 0$ eV are pairwise mirror images of each other, each pair being associated with a different quantum number μ (see equation (10)). The highest subband corresponds to $\mu = 0$; μ increases sequentially for the next lower subbands, and the lowest subband above the Fermi level corresponds to $\mu = 10$.

mode as a function of the transfer momentum is similar to the one observed by Taverna *et al* [48] in the context of the spatially resolved EELS experiment. For $L = 1$ there are no peaks at energy values below 1 eV and the behaviour of the amplitude of the loss function is similar to the $L = 0$ case. The next panels show the cases of the metallic (13, 7) and the semiconducting (16, 3) chiral nanotubes. The latter is one of the nanotubes with the smallest Brillouin zone; the edge is at $q_0 = 0.041$ Å^{-1}. The amplitude of the loss function for these chiral nanotubes is one order of magnitude smaller when compared with those for armchair and zigzag tubes. For $L = 0$ the loss functions present a sharp peak at energies in the interval 0–0.5 eV for the metallic tube and at 0.5–1 eV for the semiconducting one. In the first case the amplitude of the peak increases when the transfer momentum q_0 increases, reaches a maximum and then decreases as q_0 goes to the edge of the Brillouin zone; in contrast for the second case the amplitude of the low-energy peak always increases as the transfer momentum increases. The loss function of the metallic tube has two very distinctive peaks at energies in the interval 2–4 eV whose amplitude increases as the transfer momentum increases. In the semiconducting case there is a shoulder at energies between 1 and 2 eV and a small peak in the energy range 2–3 eV. For $L = 1$ in both cases there is only one distinctive isolated peak with energy close to 6 eV. The two lower panels of figure 4 show the cases of the semiconducting (17, 0) and the metallic (18, 0) zigzag tubes, and we see that when the transfer momentum increases the peaks also shift to higher energy, but the peak amplitudes keep growing as q_0 goes to the edge of the Brillouin zone, reaching their largest amplitude for $q_0 = 0.73$ Å^{-1} and excitation energy $\omega \sim 10$ eV. This behaviour for zigzag tubes is general and is the same whether they are metallic or semiconducting (see for example figure 2(b) of the paper by Lin *et al* [34] for a semiconducting nanotube (23, 0) with radius $R = 9$ Å). This behaviour could be used in a momentum-dependent EELS experiment for the identification of zigzag tubes. For $L = 1$ the behaviour of the loss function is very similar to the $L = 0$ case, with the remarkable exception that there is no low-energy peak in
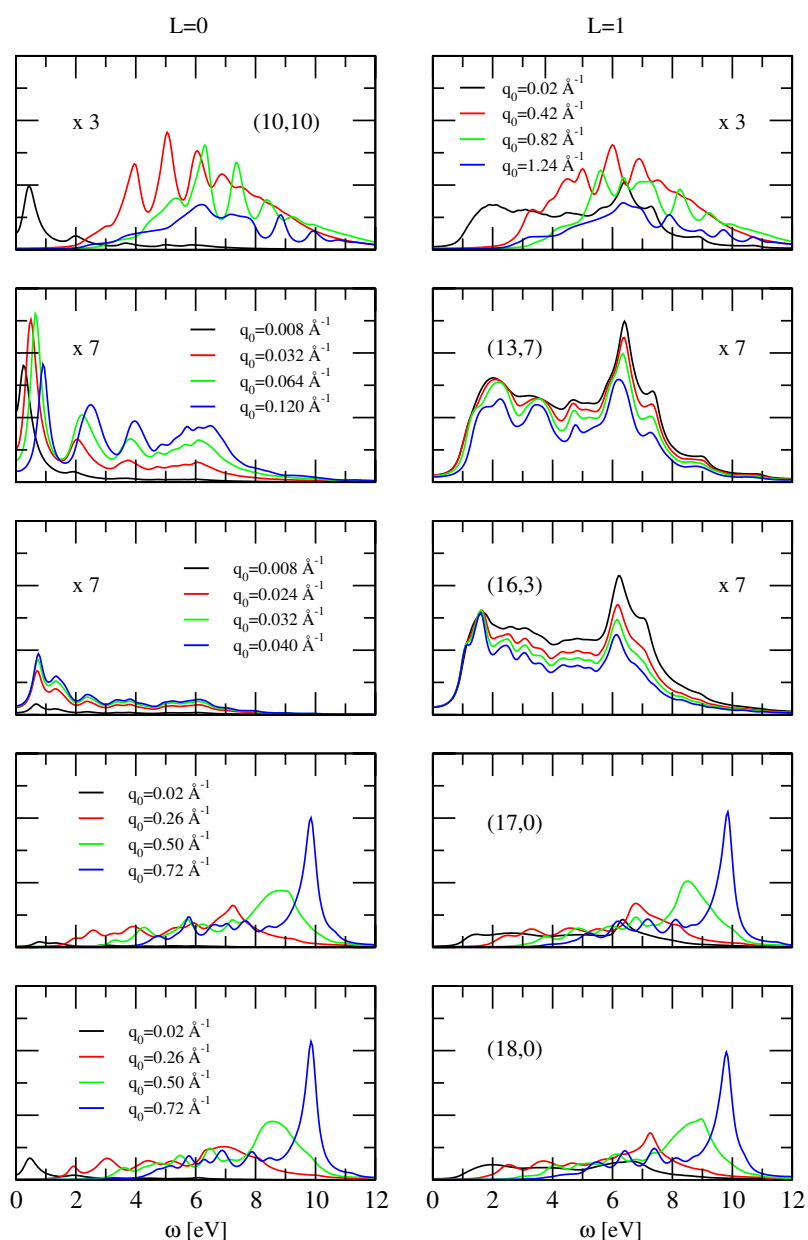
Figure 4. Loss function for armchair (10, 10), chiral (13, 7), (16, 3) and zigzag (17, 0), (18, 0) nanotubes with angular momenta $L = 0, 1$ and different transfer momentum q_0 within the first Brillouin zone. Note that the amplitudes of the loss functions have been amplified for the two chiral tubes.

any case. For small q_0, the loss functions for nanotubes of different chiralities but similar radii and electronic properties (whether they are semiconducting or metallic) are very similar.

According to the general EELS theory [49], valid for homogeneous and crystalline systems, the peaks in the loss function should be interpreted as collective excitation modes.
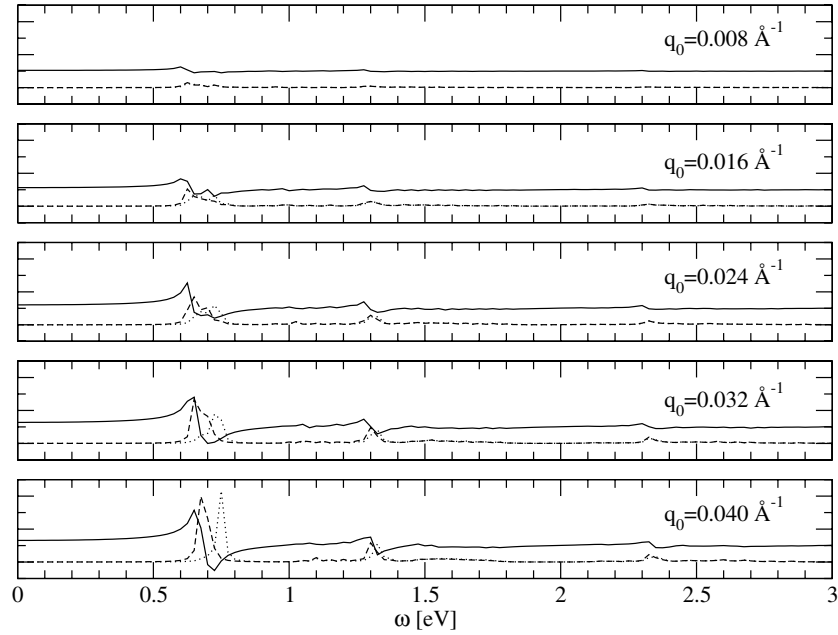
Figure 5. Plasmon modes for the semiconducting nanotube $(16, 3)$ with $L = 0$ and different transfer momenta within the Brillouin zone. The continuous (dashed) line shows the real (imaginary) part of the macroscopic dielectric function; the dotted line is the loss function. The value of $\Gamma = 0.01$ eV was used for these calculations.

For a transmission EELS experiment [50] the peaks are located at the energy ω where the real part of the macroscopic dielectric function is zero and its imaginary part is small. The imaginary part of the dielectric function provides a measure of the probability of interband transitions and its magnitude is related to the damping of the collective excitation modes: the larger the magnitude of the imaginary part of the dielectric function the larger the width of the peaks in the loss function. Figure 5 shows the real and imaginary parts of the macroscopic dielectric function and the calculated loss function for $L = 0$ excitations and different values of the transfer momentum q_0 within the 1BZ for the semiconducting $(16, 3)$ nanotube and for excitation energies up to 3 eV, the energy region where the nondispersive peaks are observed in the experiment. All the general features regarding the theory of collective excitations are clearly shown in this figure. At small transfer momentum ($q_0 = 0.008$ Å^{-1}) it is not possible to distinguish between the curve for the imaginary part of the dielectric function and the loss function, these showing a very weak and wide peak at energy close to 0.62 eV, the expected position for the first absorption peak for semiconducting nanotubes within the tight-binding model (e.g. $E_{11}^S = a_0 \gamma_0 / R$) [12], and the real part of the dielectric function has no zero. As the transfer momentum is increased towards the edge of the Brillouin zone, the real part of the dielectric function starts developing a zero in the region where its imaginary part is small and a clear difference, given by a nonzero depolarization shift, is seen between the position for the peaks of the loss function (plasmon mode) and the position of the peaks for the imaginary part of $\epsilon(q_0, L, \omega)$. Another plasmonic peak is observed at energies above 1.3 eV with an amplitude smaller than the one observed at lower energy but with a wider width.

The plasmon mode dispersion relations were obtained by scanning the loss functions as a function of energy to find peak positions for different q_0 values, and the differences between
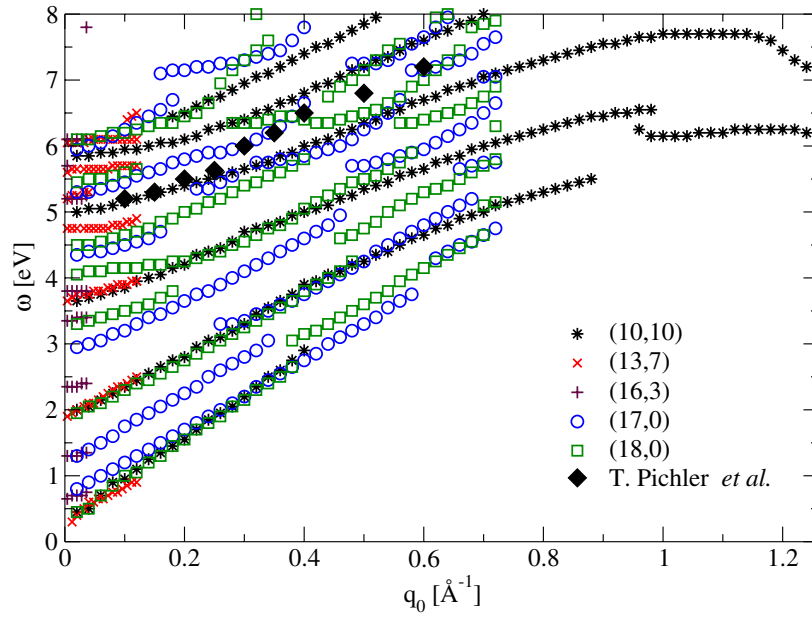
Figure 6. Dispersion relations for the plasmon modes for nanotubes with different chiralities for
angular momentum $L = 0$. The circles represent our theoretical results for isolated SWNTs, and
the diamonds are experimental data from Pichler *et al* [7] for a carbon nanotube bundle.

carbon nanotubes of different chirality became evident. In figures 6 and 7 we show the plasmon
dispersion relations for carbon nanotubes of different chiralities but similar radius $R \sim 7$ Å,
with q_0 varying from zero to the edge of their first Brillouin zone π/T and angular momenta
$L = 0, 1$. Since we are only interested in the low-energy excitation modes there is no need to
analyse excitations with higher angular momentum, as shown before. It is very obvious that
the (10, 10) armchair nanotube and the (17, 0) and (18, 0) zigzag nanotubes have plasmons
with considerable dispersion; in contrast, the chiral nanotubes (13, 7) and (16, 3) have little
dispersion. In general, all achiral tubes have plasmons with considerable dispersion. Plasmons
in chiral nanotubes have much less dispersion, and are essentially dispersionless in those chiral
tubes for which the greatest common divisor $\gcd(2n + m, 2m + n) = 1$. The different sizes
of the first Brillouin zone play an important role here. Some of the branches terminate before
reaching the Brillouin zone boundary. That is because either in these modes the amplitude of
the loss function decreases as q_0 increases or as q_0 increases the peak defining the mode merge
with another peak at higher energy, and eventually no well defined peak can be detected. The
lowest branch for the (10, 10) tube in figure 6 behaves like this. The (10, 10) tube is metallic,
and its lowest branch is an acoustic plasmon mode for $L = 0$. The (13, 7) and the (18, 0) tubes
are also metallic and have an acoustic branch. The existence of the acoustic mode is supported
by experiments. The Raman scattering experiments of Brown *et al* [16] and Jiang *et al* [17]
suggest that in metallic carbon nanotubes there is a π band conduction electron plasmon with
energy less than 0.19 eV. The reflectivity data of Bommeli *et al* [18] suggest a plasmon energy
of 0.14 eV. Such low-energy plasmons can be explained by the acoustic plasmon mode, which
arises from the subbands crossing the Fermi level. Using a free electron gas model, Kempa [28]
has argued that the optical phonon–acoustic plasmon coupling is responsible for the Breit–
Wigner–Fano line shape feature just below the tangential G-band peak in the Raman spectra of
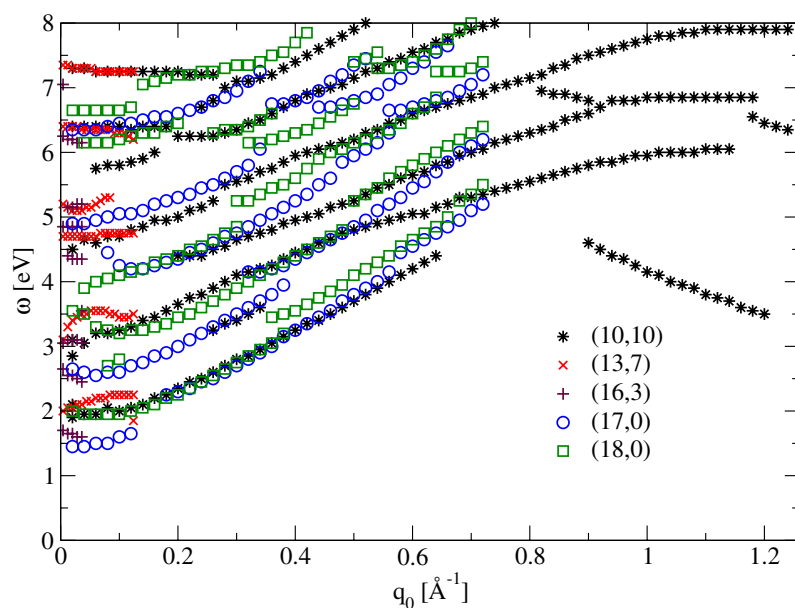
Figure 7. Similar to figure 6 but for excitations with angular momentum $L = 1$.

metallic SWNTs. All the obtained plasmon modes for the semiconducting nanotubes (16, 3) and (17, 0) are identified as optical plasmons; in this case, no subband crosses the Fermi level.

Our results offer some insights to understand the controversial origin of the low-energy modes observed in the momentum-dependent EELS experiment performed by Pichler *et al* [7, 8]. The two principal findings in the experiment were (i) a dispersive mode, interpreted as a π plasmon, with energy varying in the range 5–8 eV as a function of the transfer momentum (this mode is shown as black diamonds in figure 6) and (ii) several nondispersive modes at lower energies: 0.85, 1.45, 2.0, and 2.55 eV. Without any theoretical guidance at that time, the authors interpreted the low-energy, nondispersive modes as interband (intersubband) excitations between localized states polarized perpendicular to the nanotube axis [7]. This first interpretation was refined later in the light of new results coming from optical absorption measurements, and in a recent paper by Liu *et al* [12] it was suggested that the observed nondispersive modes are due to collective excitations of the optically allowed transitions. Although this interpretation seems to be more adequate, still no explanation was given about the nondispersive character of the observed modes.

An attempt to clarify the origin of the nondispersive modes was made by Bose [26] three years after the initial experiment, based on a calculation of a free electron gas model. The author pointed out that these low-energy modes could be optical plasmons corresponding to nonzero angular momentum L. However, the theoretical results suggested that these modes are not completely dispersionless. Although in his paper Bose did not present the calculated dispersions of the $L \neq 0$ modes, such dispersions were presented in an earlier paper with his collaborator Longe [21], with figure 1 of that paper showing the $L = 0$ mode with the most dispersion, and other modes with less and less dispersion as L increases. The amount of dispersion is still significant for the $L \neq 0$ modes, in contrast to the experimental result. A close inspection of the theoretical results reveals difficulties with the proposed interpretation. If one attributes the measured dispersive mode as the $L = 0$ plasmon, then, according to the

theory, the optical plasmons should have *higher* energies than the dispersive mode; this trend is opposite to the one observed in the experiment. If one attributes the measured dispersive mode as an $L \neq 0$ plasmon with a high L value, then the trend of the amount of dispersion as a function of L again puts theory and experiment in opposition. Therefore, while Bose pointed out an alternative explanation for the experimentally observed nondispersive low-energy modes, the theoretical qualitative features are in conflict with experiment.

Comparing the results in figures 6 and 7 with results of Longe and Bose [21], a major difference is that in the latter there is only one branch of collective mode for each angular momentum index L, while in our results we find many branches for each angular momentum. This can be understood based on the band structure of the carbon nanotubes with many occupied and many empty (sub)bands. An agreement with the predictions of the electron gas model is reached regarding the qualitative behaviour of the modes when the angular momentum L is increased; the excitation energies increase and the dispersion is reduced. Unlike Bose's, our results offer a very plausible qualitative explanation of the experimental results and there is no need to mention any specific angular momentum to explain the nondispersive character of the low-energy modes. Since the experiments were performed on a bulk sample, it should contain carbon nanotubes of various chiralities. The measured dispersive mode could be contributions from armchair and zigzag tubes, while the measured nondispersive modes could be due to chiral tubes.

Our results still do not explain the experiment perfectly: the theory predicts many branches of dispersive π plasmon modes, while experiment observed only one dispersive π plasmon mode. One possibility is that the broad peak observed experimentally is due to several peaks merged together. Also, it is not clear which chiral tubes contributed to the low-energy modes at 0.85, 1.45, 2.0, and 2.55 eV. The presence of intertube interaction in the experimental sample, which is known to shift the energy of plasmons in a model calculation [30], makes a detailed comparison of energies between the present theory and experiment difficult. Difficulties for the comparison also arise regarding the angular momentum dependence of the excitations, which is typical of isolated nanotubes and has no analogue in bundles. We believe that experiments on isolated carbon nanotubes will make a crucial contribution in our understanding of the affairs, allowing a direct comparison between theory and experiment. EELS experiment on isolated SWNTs have already been carried out by Reed and Sarikaya [10]; however, this was not a momentum-dependent measurement. They have noticed that different single tubes showed somewhat different results, consistent with our prediction that plasmons in nanotubes of different chirality behave differently.

5. Conclusion

While obviously more experiments are needed to understand plasmons in carbon nanotubes, especially momentum-dependent EELS on individual carbon nanotubes, more theoretical studies are required as well. In the present work, we have only considered the π electrons and have neglected the σ electrons. Inclusion of the σ electrons will allow us not only to study the π plasmon modes, but the $\pi + \sigma$ plasmon modes as well. Furthermore, while we have used the nearest-neighbour tight-binding approximation, the recent band structure work of Reich *et al* [51] suggests that inclusion up to third-nearest neighbours may be necessary. A known fact is that the *zone folding model* does not account properly for the curved geometry of the carbon nanotube lattice. Calculations of the collective electronic mode dispersion relations using the improved tight-binding schemes for carbon nanotubes recently proposed by Popov [52] and Zang [53] are currently in progress. Extensions of the present work to multiwalled carbon nanotubes and bundles are also needed. It is well accepted that in a metallic single-wall carbon

nanotube electrons form a Luttinger liquid [54]. Recently, it has been shown that the random phase approximation approach, as used here, describes the plasmon excitation in the Luttinger liquid of a metallic carbon nanotube correctly, consistent with the result obtained by other well established methods for Luttinger liquids [55]. Since single-particle excitations are forbidden in a Luttinger liquid, the low-energy acoustic plasmon mode in a metallic carbon nanotube cannot be Landau damped. It is not clear if the Luttinger liquid picture still holds for a carbon nanotube bundle. Calculations [30] for a carbon nanotube bundle based on a free electron gas model without invoking the Luttinger liquid picture show that plasmons in a carbon nanotube bundle are not Landau damped. The lack of Landau damping, whether due to Luttinger liquid behaviour or not, may offer an explanation for the recent experiment by Lu *et al* [56], in which an evanescent wave generated by a totally reflected photon at one boundary is shown to be able to couple to the surface plasmon at a surface several microns away via a carbon nanotube bundle layer.

The results of this work clearly demonstrate that free electron gas or hydrodynamic type models are insufficient to understand some of the important qualitative features of plasmons in carbon nanotubes. While the chirality is previously known to have an important effect on the band structure of carbon nanotubes, it has been noted for the first time here that it also has an important effect on the collective electronic excitations in carbon nanotubes. Chiral nanotubes with very small Brillouin zones can have dispersionless plasmon modes, offering an alternative explanation to the dispersionless low energy modes observed experimentally. The acoustic plasmon modes in metallic carbon nanotubes support the Raman scattering experimental results.

Acknowledgments

Appendix A. Fourier transform

The Coulomb potential is given in cylindrical coordinates by the following expression [57]:

$$\frac{1}{|\vec{r} - \vec{r}'|} = \frac{2}{\pi} \sum_{m=-\infty}^{\infty} \int_0^{\infty} dk \, e^{im(\phi - \phi')} \cos[k(z - z')] I_m(k\rho_<) K_m(k\rho_>) \tag{A.1}$$

where I_m and K_m are the modified Bessel functions of the first and second kinds, and $\rho_{< (>)}$ means the smaller (larger) radius between ρ and ρ'.

To obtain the 1D Fourier transform of the Coulomb interaction we need to perform the following integral:

$$\tfrac{1}{2} \int_{-\infty}^{\infty} e^{iqz} \left[e^{ik(z-z')} + e^{-ik(z-z')} \right] dz = \pi \left[e^{-ikz'} \delta(q+k) + e^{ikz'} \delta(q-k) \right]$$

where q is a linear momentum along the nanotube axis. Performing the integration over k in the expression for the Coulomb potential and taking into account the sign of q, we obtain for the 1D Fourier transform of the Coulomb potential the expression

$$\int_{-\infty}^{\infty} \frac{e^{iqz}}{|\vec{r} - \vec{r}'|} dz = v_q(\vec{\rho}', \vec{\rho}) e^{i|q|z'}, \tag{A.2}$$

where

$$v_q(\vec{\rho}', \vec{\rho}) = 2 \sum_{m=-\infty}^{\infty} e^{im(\phi-\phi')} I_m(|q|\rho_<) K_m(|q|\rho_>). \tag{A.3}$$

Now if we multiply $v_q(\vec{\rho}', \vec{\rho})$ by $e^{iL\phi}$ and perform the ϕ-integration we obtain

$$\int_0^{2\pi} v_q(\vec{\rho}', \vec{\rho}) e^{iL\phi} \, d\phi = 2 \sum_{m=-\infty}^{\infty} e^{-im\phi'} I_m(|q|\rho_<) K_m(|q|\rho_>) \int_0^{2\pi} e^{i(m+L)\phi} \, d\phi,$$

using the relations [58]

$$I_{-L}(z) = I_L(z) \tag{A.4}$$
$$K_{-L}(z) = K_L(z) \tag{A.5}$$

we get the final expression

$$\int_0^{2\pi} v_q(\vec{\rho}', \vec{\rho}) e^{iL\phi} \, d\phi = 4\pi F(\rho', \rho, q, L) e^{iL\phi'}, \tag{A.6}$$

where $F(\rho', \rho, q, L) = I_L(|q|\rho_<) K_L(|q|\rho_>)$.

Appendix B. Matrix element between tight-binding functions

In this appendix we compute the matrix element $\langle h'\vec{k} + \vec{q}_0 | e^{i(\vec{q}_0+\vec{G})\cdot\vec{r}} | h\vec{k} \rangle$ between the tight-binding wavefunctions (5)

$$\langle h'\vec{k} + \vec{q}_0 | e^{i(\vec{q}_0+\vec{G})\cdot\vec{r}} | h\vec{k} \rangle = \frac{1}{2} \int \left\{ \left[\Phi_{\vec{k}+\vec{q}_0}^A(\vec{r}) + \lambda_{\vec{k}+\vec{q}_0}^{h'} \Phi_{\vec{k}+\vec{q}_0}^B(\vec{r}) \right]^* e^{i(\vec{q}_0+\vec{G})\cdot\vec{r}} \right.$$
$$\left. \times \left[\Phi_{\vec{k}}^A(\vec{r}) + \lambda_{\vec{k}}^h \Phi_{\vec{k}}^B(\vec{r}) \right] \right\} d^3r.$$

Since $\Phi_{\vec{k}}^{A,B}(\vec{r})$ are localized functions, we use the approximation

$$\int \Phi_{\vec{k}+\vec{q}_0}^\alpha(\vec{r})^* e^{i(\vec{q}_0+\vec{G})\cdot\vec{r}} \Phi_{\vec{k}}^\beta(\vec{r}) \, d^3r = 0 \tag{B.1}$$

for all $\alpha \neq \beta$. Hence

$$\langle h'\vec{k} + \vec{q}_0 | e^{i(\vec{q}_0+\vec{G})\cdot\vec{r}} | h\vec{k} \rangle = \frac{1}{2} \left\{ \int \Phi_{\vec{k}+\vec{q}_0}^A(\vec{r})^* e^{i(\vec{q}_0+\vec{G})\cdot\vec{r}} \Phi_{\vec{k}}^A(\vec{r}) \, d^3r \right.$$
$$\left. + \lambda_{\vec{k}+\vec{q}_0}^{h'*} \lambda_{\vec{k}}^h \int \Phi_{\vec{k}+\vec{q}_0}^B(\vec{r})^* e^{i(\vec{q}_0+\vec{G})\cdot\vec{r}} \Phi_{\vec{k}}^B(\vec{r}) \, d^3r \right\}.$$

The integrals in both terms on the r.h.s. are very similar. Now we give the steps to compute the first of them:

$$\int \Phi_{\vec{k}+\vec{q}_0}^A(\vec{r})^* e^{i(\vec{q}_0+\vec{G})\cdot\vec{r}} \Phi_{\vec{k}}^A(\vec{r}) \, d^3r = \frac{1}{N} \frac{1}{N_0} \sum_{\beta,\beta'=1}^{N} \sum_{\gamma,\gamma'=1}^{N_0} e^{-i(\vec{k}+\vec{q}_0)\cdot\vec{R}_{\beta'}^A + i\vec{k}\cdot\vec{R}_\beta^A}$$
$$\times e^{-i(\vec{k}+\vec{q}_0)\cdot\vec{\tau}_{\gamma'} + i\vec{k}\cdot\vec{\tau}_\gamma} \int \phi_{2p_z}^*(\vec{r} - \vec{R}_{\beta'}^A - \vec{\tau}_{\gamma'}) e^{i(\vec{q}_0+\vec{G})\cdot\vec{r}}$$
$$\times \phi_{2p_z}(\vec{r} - \vec{R}_\beta^A - \vec{\tau}_\gamma) \, d^3r. \tag{B.2}$$

Defining $\vec{r}' = \vec{r} - \vec{R}_{\beta'}^{A} - \vec{\tau}_{\gamma'}$, we have

$$\int \Phi_{\vec{k}+\vec{q}_0}^{A}(\vec{r})^* e^{i(\vec{q}_0+\vec{G})\cdot\vec{r}} \Phi_{\vec{k}}^{A}(\vec{r}) \, d^3r = \frac{1}{N}\frac{1}{N_0} \sum_{\beta,\beta'=1}^{N} \sum_{\gamma,\gamma'=1}^{N_0} e^{-i(\vec{k}+\vec{q}_0)\cdot\vec{R}_{\beta'}^{A}+i\vec{k}\cdot\vec{R}_{\beta}^{A}+i(\vec{q}_0+\vec{G})\cdot\vec{R}_{\beta'}^{A}}$$

$$\times e^{-i(\vec{k}+\vec{q}_0)\cdot\vec{\tau}_{\gamma'}+i\vec{k}\cdot\vec{\tau}_{\gamma}+i(\vec{q}_0+\vec{G})\cdot\vec{\tau}_{\gamma'}} \int \phi_{2p_z}^*(\vec{r}') e^{i(\vec{q}_0+\vec{G})\cdot\vec{r}'}$$

$$\times \phi_{2p_z}(\vec{r}' + \vec{R}_{\beta'}^{A} - \vec{R}_{\beta}^{A} + \vec{\tau}_{\gamma'} - \vec{\tau}_{\gamma}) \, d^3r' \tag{B.3}$$

and due to the localized character of the atomic orbitals $\phi_{2p_z}(\vec{r})$ we get

$$\int \phi_{2p_z}^*(\vec{r}') e^{i(\vec{q}_0+\vec{G})\cdot\vec{r}'} \phi_{2p_z}(\vec{r}' + \vec{R}_{\beta'}^{A} - \vec{R}_{\beta}^{A} + \vec{\tau}_{\gamma'} - \vec{\tau}_{\gamma}) \, d^3r' = A(\vec{q}_0 + \vec{G})\delta_{\beta\beta'}\delta_{\gamma\gamma'}$$

where we have defined

$$A(\vec{q}) = \int \phi_{2p_z}^*(\vec{r}') e^{i\vec{q}\cdot\vec{r}'} \phi_{2p_z}(\vec{r}') \, d^3r'. \tag{B.4}$$

Now we can do exactly the sum over β, β', γ'

$$\int \Phi_{\vec{k}+\vec{q}_0}^{A}(\vec{r})^* e^{i(\vec{q}_0+\vec{G})\cdot\vec{r}} \Phi_{\vec{k}}^{A}(\vec{r}) \, d^3r = \frac{A(\vec{q}_0 + \vec{G})}{N_0} \sum_{\gamma=1}^{N_0} e^{i\vec{G}\cdot\vec{\tau}_{\gamma}} \tag{B.5}$$

where $\vec{G}$ is a vector in the nanotube's reciprocal lattice ($\vec{G} = g\vec{K}_2$). Recalling that $\vec{\tau}_{\gamma} = (\gamma - 1)\vec{R} - r_{\gamma}\vec{T}$ where r_{γ} is an integer then

$$\vec{G}\cdot\vec{\tau}_{\gamma} = 2\pi(\gamma-1)\frac{g}{N_0}(mp_1 - np_2) - 2\pi g r_{\gamma}$$

$$= 2\pi(\gamma-1)\frac{g}{N_0}M - 2\pi g r_{\gamma}. \tag{B.6}$$

Doing the sum over γ we obtain

$$\frac{1}{N_0} \sum_{\gamma=1}^{N_0} e^{i\vec{G}\cdot\vec{\tau}_{\gamma}} = \frac{1}{N_0} \left[\frac{e^{2\pi i g M} - 1}{e^{2\pi i \frac{g}{N_0} M} - 1} \right]. \tag{B.7}$$

The expression between square brackets is zero if $gM \neq uN_0$ and is unity if $gM = uN_0$ for any integer u. The physical meaning of this condition is easy to visualize: the vectors $\vec{\tau}_{\gamma}$ giving the carbon atom positions in the nanotube's unit cell belong to the direct lattice of the underlying graphene layer, but in general a vector $\vec{G}$ in the reciprocal lattice of the nanotube does not belong to the underlying graphene reciprocal lattice. Only those vectors $\vec{G}$ which satisfy the condition $gM = uN_0$ belong to both reciprocal lattices and their contribution in equation (B.5) is nonzero. This is an intrinsic drawback of the *zone folding method*, no matter how many neighbours one includes in the tight-binding calculation or how many atomic orbitals are considered.

The way to compute the integral in the second term is the same; the only difference in the result is an additional phase $e^{i\vec{G}\cdot\vec{\ell}_{AB}}$ coming from the displacement between the lattice of atoms A and B.

Finally, we obtain the expression for the matrix element as

$$\langle h'\vec{k} + \vec{q}_0 | e^{i(\vec{q}_0+\vec{G})\cdot\vec{r}} | h\vec{k} \rangle = \frac{1}{2} \left(1 + e^{i\vec{G}\cdot\vec{\ell}_{AB}} \lambda_{\vec{k}+\vec{q}_0}^{h'*} \lambda_{\vec{k}}^{h} \right) A(\vec{q}_0 + \vec{G})\delta_{gM,uN_0}$$

where the expression $A(\vec{q}) = \langle 2p_z | e^{i\vec{q}\cdot\vec{r}} | 2p_z \rangle$ is calculated in the following appendix.

Appendix C. $A(\vec{q})$ function

We need to compute the matrix element $\langle 2p_z|\mathrm{e}^{\mathrm{i}\vec{q}\cdot\vec{r}}|2p_z\rangle$. Here $\vec{q}$ is a vector in the x–y plane and the atomic orbitals $|2p_z\rangle$ are given by the following expression:

$$\langle\vec{r}|2p_z\rangle = \phi_{2p_z}(\vec{r}) = \frac{Z^{5/2}}{4\sqrt{2\pi}a_0^{5/2}}r\cos\theta\,\mathrm{e}^{-Zr/2a_0}, \tag{C.1}$$

where $Z = 3.18$ is the effective atomic number and $a_0 = 0.529\,177$ Å is the Bohr radius [59]. The matrix element we are interested in is given in cylindrical coordinates $\vec{r} = (\vec{\rho}, z)$ by the integral

$$\langle 2p_z|\mathrm{e}^{\mathrm{i}\vec{q}\cdot\vec{r}}|2p_z\rangle = C^2\int\mathrm{d}^2\rho\,\mathrm{e}^{\mathrm{i}\vec{q}\cdot\vec{\rho}}\int_{-\infty}^{\infty}\mathrm{d}z\,z^2\mathrm{e}^{-Z\sqrt{\rho^2+z^2}/a_0}$$

where we have used the relation $z = r\cos\theta$ and $C = \frac{Z^{5/2}}{4\sqrt{2\pi}a_0^{5/2}}$. In the z integral, since the integrand is an even function of z, we can change the lower limit of the integral to zero and multiply the result by two. With the variable change $u = \sqrt{\rho^2 + z^2}$ we transform our integral to

$$\int_{-\infty}^{\infty}\mathrm{d}z\,z^2\mathrm{e}^{-Z\sqrt{\rho^2+z^2}/a_0} = 2\int_{\rho}^{\infty}\mathrm{d}u\,u\sqrt{u^2-\rho^2}\mathrm{e}^{-Zu/a_0}.$$

Using the table of integrals [58] we get

$$\int_{-\infty}^{\infty}\mathrm{d}z\,z^2\mathrm{e}^{-Z\sqrt{\rho^2+z^2}/a_0} = \frac{4}{\sqrt{\pi}}\frac{a_0}{Z}\Gamma(3/2)\rho^2 K_2(Z\rho/a_0) \tag{C.2}$$

where K_2 is the modified Bessel function.

Now taking an arbitrary vector $\vec{q}$ of length q and forming an angle ϕ' with the x axis, we get the scalar product $\vec{q}\cdot\vec{\rho} = q\rho\cos(\phi - \phi')$. So far we have

$$\langle 2p_z|\mathrm{e}^{\mathrm{i}\vec{q}\cdot\vec{r}}|2p_z\rangle = C^2\frac{4}{\sqrt{\pi}}\frac{a_0}{Z}\Gamma(3/2)\int_0^{\infty}\mathrm{d}\rho\,\rho^3 K_2(Z\rho/a_0)\int_0^{2\pi}\mathrm{d}\phi\,\mathrm{e}^{\mathrm{i}q\rho\cos(\phi-\phi')}. \tag{C.3}$$

To evaluate the integral on the angular variable, we start by expanding the exponential function

$$\int_0^{2\pi}\mathrm{d}\phi\,\mathrm{e}^{\mathrm{i}q\rho\cos(\phi-\phi')} = \sum_{t=0}^{\infty}\frac{(\mathrm{i}q\rho)^t}{t!}\int_0^{2\pi}\mathrm{d}\phi\,\cos^t(\phi-\phi') \tag{C.4}$$

to obtain the result [58]

$$\int_0^{2\pi}\mathrm{d}\phi\,\mathrm{e}^{\mathrm{i}q\rho\cos(\phi-\phi')} = 2\pi\sum_{m=0}^{\infty}(-1)^m\frac{(q\rho)^{2m}}{(2m)!!^2} \tag{C.5}$$

where $(2m)!! = 2\cdot 4\cdots 2m = 2^m m!$ and finally arrive at the expression

$$\int_0^{2\pi}\mathrm{d}\phi\,\mathrm{e}^{\mathrm{i}q\rho\cos(\phi-\phi')} = 2\pi\sum_{m=0}^{\infty}(-1)^m\frac{(q\rho)^{2m}}{2^{2m}m!^2} = 2\pi J_0(q\rho). \tag{C.6}$$

From the steps above and using $\Gamma(3/2) = \sqrt{\pi}/2$, the matrix element becomes

$$\langle 2p_z|\mathrm{e}^{\mathrm{i}\vec{q}\cdot\vec{r}}|2p_z\rangle = C^2 4\pi\frac{a_0}{Z}\int_0^{\infty}\mathrm{d}\rho\,\rho^3 K_2(Z\rho/a_0)J_0(q\rho),$$

where [58]

$$\int_0^{\infty}\mathrm{d}\rho\,\rho^3 K_2(Z\rho/a_0)J_0(q\rho) = \frac{8(Z/a_0)^2}{(q^2+(Z/a_0)^2)^3}. \tag{C.7}$$

Putting all together we arrive at our final expression

$$A(\vec{q}) = \langle 2p_z|\mathrm{e}^{-\mathrm{i}\vec{q}\cdot\vec{r}}|2p_z\rangle = \left(1+\frac{a_0^2}{Z^2}q^2\right)^{-3}. \tag{C.8}$$

References

[1] Iijima S 1991 *Nature* **354** 56
[2] Dresselhaus M S and Dresselhaus G 2001 *Carbon Nanotubes: Synthesis, Structure, Properties and Applications* (Berlin: Springer)
[3] Saito R, Dresselhaus G and Dresselhaus M S 1998 *Physical Properties of Carbon Nanotubes* (London: Imperial College Press)
[4] Kuzuo R *et al* 1992 *Japan. J. Appl. Phys.* **31** L1484
[5] Ajayan P M *et al* 1993 *Phys. Rev.* B **47** 6859
[6] Bursill L A *et al* 1994 *Phys. Rev.* B **49** 2882
[7] Pichler T *et al* 1998 *Phys. Rev. Lett.* **80** 4729
[8] Knupfer M *et al* 1999 *Carbon* **37** 733
[9] Kociak M *et al* 2000 *Phys. Rev.* B **61** 13936
[10] Reed B W and Sarikaya M 2001 *Phys. Rev.* B **64** 195404
[11] Liu X *et al* 2001 *Synth. Met.* **121** 1183
[12] Liu X *et al* 2002 *Phys. Rev.* B **66** 045411
[13] Stöckli T *et al* 2002 *Appl. Phys. Lett.* **80** 2982
[14] Stephan O *et al* 2002 *Phys. Rev.* B **66** 155422
[15] Liu X *et al* 2003 *Phys. Rev.* B **67** 125403
[16] Brown S D M *et al* 2001 *Phys. Rev.* B **63** 155414
[17] Jiang C *et al* 2002 *Phys. Rev.* B **66** 161404
[18] Bommeli F *et al* 1996 *Solid State Commun.* **99** 513
[19] Lin M F and Shung W K 1993 *Phys. Rev.* B **47** 6617
[20] Sato O *et al* 1993 *Phys. Rev.* B **48** 1947
[21] Longe P and Bose S M 1993 *Phys. Rev.* B **48** 18239
[22] Yannouleas C *et al* 1994 *Phys. Rev.* B **50** 7977
[23] Davids P S *et al* 1994 *Phys. Rev.* B **49** 5682
[24] Jiang X 1996 *Phys. Rev.* B **54** 13487
[25] Vasvari B 1997 *Phys. Rev.* B **55** 7993
[26] Bose S M 2001 *Phys. Lett.* A **289** 255
[27] Stöckli T *et al* 2001 *Phys. Rev.* B **64** 115424
[28] Kempa K 2002 *Phys. Rev.* B **66** 195406
[29] Taverna D *et al* 2003 *J. Electron Spectrosc. Relat. Phenom.* **129** 293
[30] Que W 2002 *J. Phys.: Condens. Matter* **14** 5239
[31] Adler S L 1962 *Phys. Rev.* **126** 413
[32] Wiser N 1963 *Phys. Rev.* **129** 62
[33] Lin M F and Shung W K 1994 *Phys. Rev.* B **50** 17744
[34] Lin M F *et al* 1996 *Phys. Rev.* B **53** 15493
[35] Lin M F *et al* 1997 *Phys. Rev.* B **56** 1430
[36] Shyu F L and Lin M F 2000 *Phys. Rev.* B **62** 8508
[37] Marinopoulos A G *et al* 2003 *Phys. Rev. Lett.* **91** 046402
[38] Marinopoulos A G *et al* 2004 *Appl. Phys.* A **78** 1157
[39] Lefebvre J *et al* 2004 *Phys. Rev.* B **69** 075403
[40] Hartschuh A *et al* 2003 *Phys. Rev. Lett.* **90** 095503
[41] Perez R and Que W 2005 *J. Phys.: Condens. Matter* **17** L367
[42] Que W and Kirczenow G 1989 *Phys. Rev.* B **39** 5998
     Que W 1991 *Phys. Rev.* B **43** 7127
     Li Q P and Das Sarma S 1991 *Phys. Rev.* B **43** 11768
[43] Ehrenreich H and Cohen M H 1959 *Phys. Rev.* **115** 786
[44] Slater J C and Koster G F 1954 *Phys. Rev.* **94** 1498
[45] Saito R *et al* 1992 *Phys. Rev.* B **46** 1804
[46] Benedict L X *et al* 1995 *Phys. Rev.* B **52** 8541
[47] Chang E *et al* 2004 *Phys. Rev. Lett.* **92** 196401
[48] Taverna D *et al* 2002 *Phys. Rev.* B **66** 235419
[49] Raether H 1980 *Excitation of Plasmons and Interband Transitions by Electrons* (Berlin: Springer)
[50] Lucas A A 1992 *J. Phys. Chem. Solids* **53** 1415
[51] Reich S *et al* 2002 *Phys. Rev.* B **66** 035412
[52] Popov V N and Henrard L 2004 *Phys. Rev.* B **70** 115407

      Popov V N 2004 *New J. Phys.* **6** 17

[53] Zang M 2005 *IEEE Trans. Nanotechnol.* **4** 452

[54] Egger R and Gogolin A O 1997 *Phys. Rev. Lett.* **79** 5082

      Kane Ch *et al* 1997 *Phys. Rev. Lett.* **79** 5086

      Bockrath M *et al* 1999 *Nature* **397** 598

[55] Que W 2002 *Phys. Rev.* B **66** 193405

      Que W 2003 *Phys. Rev.* B **67** 129901

[56] Lu Q *et al* 2004 private communication

[57] Jackson J D 1999 *Classical Electrodynamics* (New York: Wiley)

[58] Gradshteyn I S and Ryzhik I M 1965 *Table of Integrals, Series and Products* (New York: Academic)

[59] Shung K W-K 1986 *Phys. Rev.* B **34** 979